

Distributional Stability of Tangent-Linearized Gaussian Inference on Smooth Manifolds

Junghoon Seo, Hakjin Lee, Jaehoon Sim

Abstract—Gaussian inference on smooth manifolds is central to robotics, but exact marginalization and conditioning are generally non-Gaussian and geometry-dependent. We study tangent-linearized Gaussian inference and derive explicit non-asymptotic W_2 stability bounds for projection marginalization and surface-measure conditioning. The bounds separate local second-order geometric distortion from nonlocal tail leakage and, for Gaussian inputs, yield closed-form diagnostics from (μ, Σ) and curvature/reach surrogates. Circle and planar-pushing experiments validate the predicted calibration transition near $\sqrt{\|\Sigma\|_{\text{op}}}/R \approx 1/6$ and indicate that normal-direction uncertainty is the dominant failure mode when locality breaks. These diagnostics provide practical triggers for switching from single-chart linearization to multi-chart or sample-based manifold inference. Code and Jupyter notebooks are available at <https://github.com/mikigom/StabilityTLGaussian>.

I. INTRODUCTION

Probabilistic inference on smooth manifolds is fundamental in robotics whenever state spaces or constraints are intrinsically nonlinear (e.g., pose/Lie groups [1], contact sets [2, 3], and kinematic manifolds [4]). In these settings, estimators must return both manifold-valued states and calibrated uncertainty for planning, control, and sensor fusion [1]. Two recurring operations are *marginalization* (eliminating nuisance directions) and *conditioning* (enforcing constraints). Although both are classical in Euclidean spaces, their manifold counterparts depend on local geometry and probability-mass locality and are not captured by linear-subspace theory alone [5]. For positive-codimension manifolds, $\{X \in \mathcal{M}\}$ has zero ambient measure, so conditioning must instead be defined by restricting the ambient density to \mathcal{M} and renormalizing with respect to surface measure, rather than by event conditioning in \mathbb{R}^n .

Recently, Guo et al. (2025) [6] derived explicit Gaussian identities for *linear* constraint manifolds and advocated a linearize–infer–retract workflow for smooth manifolds: linearize at $\tilde{\mu} \in \mathcal{M}$, apply affine-manifold identities on $T_{\tilde{\mu}}\mathcal{M}$, and map the result back to \mathcal{M} using a retraction or chart. In robotics estimation, their framework enables tight, geometry-consistent uncertainty extraction for constrained inference by performing closed-form marginalization/conditioning on tangent-space surrogates and retracting back to the manifold. This viewpoint connects to constrained covariance extraction in factor-graph systems [7], projection-based directional uncertainty models on circles and spheres [8, 9], and geometry-aware filtering on Lie groups/manifolds [10, 11, 12]. Yet the question remains: **when is a single tangent linearization**

reliable at the distribution level? This question arises concretely when propagating quaternion covariance on S^3 , extracting contact-consistent uncertainty, or enforcing SLAM loop closures. Despite the prevalence of tangent-linearized workflows in robotics estimation, no existing work provides explicit, non-asymptotic distributional error bounds that separate the roles of curvature, covariance scale, and mean offset for these operations.

In this paper, we formalize reliability as a *distributional* stability question: how close are the exact manifold-induced laws to the laws produced by tangent linearization and retraction? We quantify this discrepancy using the 2-Wasserstein distance W_2 , since it metrizes weak convergence with second moments and therefore directly controls mean and covariance errors [13, 14]. Concretely, for an ambient Gaussian $X \sim \mathcal{N}(\mu, \Sigma)$ and a C^2 embedded submanifold $\mathcal{M} \subset \mathbb{R}^n$, we take as *exact* targets the two canonical ways of pushing mass onto \mathcal{M} :

- **Marginalization via projection:** $P_{\text{marg}} := g_{\#}\mathcal{N}(\mu, \Sigma)$ where g is (locally) the Euclidean metric projection onto \mathcal{M} .
- **Conditioning via surface measure:** P_{cond} with density proportional to the ambient Gaussian density restricted to \mathcal{M} , i.e., $dP_{\text{cond}} \propto \varphi_{\mu, \Sigma} d\text{Vol}_{\mathcal{M}}$.

Given a linearization point $\tilde{\mu} \in \mathcal{M}$, its surrogate replaces \mathcal{M} by its tangent space $T_{\tilde{\mu}}\mathcal{M}$, applies the corresponding affine-manifold identities, and then maps the resulting law back to \mathcal{M} via a retraction or chart [6, 15]. Our contributions are threefold:

- We derive explicit non-asymptotic W_2 stability bounds for projection marginalization and surface-measure conditioning, decomposing error into local second-order geometric distortion and nonlocal tail leakage.
- We specialize these bounds to Gaussian inputs, yielding computable diagnostics from (μ, Σ) together with local curvature/reach surrogates.
- We validate the predicted regimes in circle and planar-pushing experiments, including anisotropy, offset, and directional-noise stress tests.

II. PRELIMINARIES

We work in the Euclidean space $(\mathbb{R}^n, \langle \cdot, \cdot \rangle)$ with norm $\|x\| := \sqrt{\langle x, x \rangle}$. For $r > 0$ and $x \in \mathbb{R}^n$, let $B(x, r) := \{z \in \mathbb{R}^n : \|z - x\| \leq r\}$ and $B(r) := B(0, r)$. For a matrix A , $\|A\|_{\text{op}}$ and $\|A\|_F$ denote the operator and Frobenius norms, respectively. We write $\mathbf{1}_A$ for the indicator of an event A . For a measurable map $h : \mathbb{R}^n \rightarrow \mathbb{R}^m$ and a probability measure P on \mathbb{R}^n , the *pushforward* is $h_{\#}P$, defined by

The authors are with AI Robot Team, PIT IN Corp., South Korea. {sjh,hj,simjeh}@pitin-ev.com

$(h_{\#}P)(B) = P(h^{-1}(B))$ for Borel $B \subset \mathbb{R}^m$. If X has law $\mathcal{L}(X) = P$, then $\mathcal{L}(h(X)) = h_{\#}P$.

Wasserstein distance: Let $\mathcal{P}_2(\mathbb{R}^n)$ be the set of Borel probability measures on \mathbb{R}^n with finite second moment. For $P, Q \in \mathcal{P}_2(\mathbb{R}^n)$, the 2-Wasserstein distance [13, 14] is

$$W_2(P, Q) := \inf_{\pi \in \Pi(P, Q)} \left(\int_{\mathbb{R}^n \times \mathbb{R}^n} \|x - y\|^2 d\pi(x, y) \right)^{1/2}, \quad (1)$$

where $\Pi(P, Q)$ denotes the set of couplings of (P, Q) . For any coupling (X, Y) with $\mathcal{L}(X) = P$ and $\mathcal{L}(Y) = Q$,

$$W_2(P, Q) \leq (\mathbb{E}\|X - Y\|^2)^{1/2}. \quad (2)$$

If $h : \mathbb{R}^n \rightarrow \mathbb{R}^m$ is L -Lipschitz,

$$W_2(h_{\#}P, h_{\#}Q) \leq L W_2(P, Q). \quad (3)$$

Moreover, W_2 controls both location ($\|\mu_P - \mu_Q\| \leq W_2(P, Q)$) and, via Cauchy–Schwarz, uncentered second-moment discrepancy ($\|M_2(P) - M_2(Q)\|_F \leq \sqrt{2(m_2(P) + m_2(Q))} W_2(P, Q)$, where $m_2(\nu) := \mathbb{E}_{Z \sim \nu} \|Z\|^2$) [16]. We therefore state our stability bounds in W_2 as practical calibration criteria for both marginalization and conditioning.

Embedded submanifolds, curvature, and reach: Let $\mathcal{M} \subset \mathbb{R}^n$ be a C^2 embedded submanifold of dimension d . For $y \in \mathcal{M}$, denote by $T_y\mathcal{M}$ its tangent space and by $N_y\mathcal{M} = (T_y\mathcal{M})^\perp$ its normal space. Let $\Pi_{T_y\mathcal{M}}$ and $\Pi_{N_y\mathcal{M}}$ be the corresponding orthogonal projectors. Write $\Pi_y : T_y\mathcal{M} \times T_y\mathcal{M} \rightarrow N_y\mathcal{M}$ for the second fundamental form. The *reach* of a closed set $S \subset \mathbb{R}^n$, $\text{reach}(S)$, is the largest ρ such that every point within distance $< \rho$ has a unique nearest point in S . If $\text{reach}(\mathcal{M}) \geq \rho > 0$, the metric projection g is well-defined on the tube $\mathcal{T}_\rho(\mathcal{M}) := \{x : \text{dist}(x, \mathcal{M}) < \rho\}$ [17].

Retractions and charts: Fix $\tilde{\mu} \in \mathcal{M}$ and write $T := T_{\tilde{\mu}}\mathcal{M}$. A (local) retraction at $\tilde{\mu}$ is a C^2 map $R_{\tilde{\mu}} : B_T(r) \rightarrow \mathcal{M}$ satisfying $R_{\tilde{\mu}}(0) = \tilde{\mu}$ and $DR_{\tilde{\mu}}(0) = \text{Id}_T$. We use a quadratic accuracy bound [15]: there exists $\kappa_R \geq 0$ such that

$$\|R_{\tilde{\mu}}(v) - (\tilde{\mu} + v)\| \leq \frac{\kappa_R}{2} \|v\|^2, \quad \|v\| \leq r. \quad (4)$$

More generally, for a chart $\Psi : B_r \subset \mathbb{R}^d \rightarrow \mathcal{M}$ with $\Psi(0) = \tilde{\mu}$, the induced volume satisfies $d\text{Vol}_{\mathcal{M}}(\Psi(v)) = J(v) dv$ [18].

A. Marginalization and conditioning onto manifolds

Let $X \in \mathbb{R}^n$ have law P with density p , and let $\mathcal{M} = \{x \in \mathbb{R}^n : f(x) = 0\}$ be a d -dimensional smooth manifold defined by a regular map $f : \mathbb{R}^n \rightarrow \mathbb{R}^{n-d}$. Following [6], there are two canonical ways to push probability onto \mathcal{M} : (i) *marginalization by projection*: choose $g_{\mathcal{M}} : \mathbb{R}^n \rightarrow \mathcal{M}$ and set

$$P_{\text{marg}} := (g_{\mathcal{M}})_{\#}P; \quad (5)$$

(ii) *conditioning*: restrict and renormalize, giving

$$dP_{\text{cond}}(x) = Z_{\mathcal{M}}^{-1} p(x) d\text{Vol}_{\mathcal{M}}(x), \quad Z_{\mathcal{M}} := \int_{\mathcal{M}} p(x) d\text{Vol}_{\mathcal{M}}(x), \quad (6)$$

assuming $0 < Z_{\mathcal{M}} < \infty$. For $\text{codim}(\mathcal{M}) > 0$, this is *not* event conditioning on $\{X \in \mathcal{M}\}$ (which has measure zero under the ambient law). It is a new probability measure obtained by restricting the density to \mathcal{M} and normalizing with respect to $\text{Vol}_{\mathcal{M}}$.

For an affine linear manifold $\mathcal{M}_{\text{lin}} := \{x \in \mathbb{R}^n : S^\top x = c\}$ with full-rank $S \in \mathbb{R}^{n \times q}$, $q < n$, let N span $\text{null}(S^\top)$ and define $\Pi := N(N^\top N)^{-1}N^\top$. For $X \sim \mathcal{N}(\mu, \Sigma)$, marginalization and conditioning admit closed forms [6]:

$$\mu_{\text{marg}} = \Pi\mu + x_0, \quad \Sigma_{\text{marg}} = \Pi\Sigma\Pi^\top, \quad (7)$$

$$\Sigma_{\text{cond}} = N(N^\top \Sigma^{-1}N)^{-1}N^\top, \quad (8)$$

$$\mu_{\text{cond}} = x_0 + \Sigma_{\text{cond}}\Sigma^{-1}(\mu - x_0),$$

where $x_0 := S(S^\top S)^{-1}c \in \mathcal{M}_{\text{lin}}$.

B. Linearization principle for smooth manifolds

The closed-form identities (7)–(8) hold when the constraint manifold is an affine subspace of \mathbb{R}^n . To extend them to a smooth nonlinear submanifold $\mathcal{M} \subset \mathbb{R}^n$, we adopt a standard *tangent-plane surrogate*: select a linearization point $\tilde{\mu} \in \mathcal{M}$ (typically the Euclidean projection of the ambient mean onto \mathcal{M} or a current estimate) and replace \mathcal{M} locally by its first-order approximation at $\tilde{\mu}$ [6]. Specifically, let $\mathcal{M} = \{x : f(x) = 0\}$ be a regular level set for a smooth $f : \mathbb{R}^n \rightarrow \mathbb{R}^{n-d}$ with $\text{rank } Df(\tilde{\mu}) = n - d$. The tangent space at $\tilde{\mu}$ then admits the affine representation

$$T_{\tilde{\mu}}\mathcal{M} = \{x \in \mathbb{R}^n : S^\top x = c\}, \quad S := Df(\tilde{\mu})^\top, \quad c := S^\top \tilde{\mu}, \quad (9)$$

where $N := \text{null}(S^\top)$ spans tangent directions and $\Pi := N(N^\top N)^{-1}N^\top$ is the orthogonal projector onto $T_{\tilde{\mu}}\mathcal{M}$. Applying (7) or (8) in this affine setting yields a *degenerate Gaussian* on $T_{\tilde{\mu}}\mathcal{M}$, constituting a first-order approximation to the on-manifold distribution.

Because tangent-space distributions do not lie on \mathcal{M} itself, the resulting Gaussian is mapped back to \mathcal{M} via a retraction $R_{\tilde{\mu}}$ or an explicit chart Ψ , producing the pushforward $\hat{P} := (R_{\tilde{\mu}})_{\#}P_T$ (or $\hat{P} := \Psi_{\#}Q_T$ in local coordinates), where P_T is the Gaussian on $T_{\tilde{\mu}}\mathcal{M}$. In what follows, we adopt this tangent–retraction construction as the baseline and derive distribution-level error bounds that quantify when a single linearization suffices.

III. W_2 STABILITY FOR GAUSSIAN MARGINALIZATION

Let $\mathcal{M} \subset \mathbb{R}^n$ be a C^2 embedded submanifold and let $X \sim \mathcal{N}(\mu, \Sigma)$ with $\Sigma \succ 0$. With $g : \mathbb{R}^n \rightarrow \mathcal{M}$ denoting a measurable nearest-point projection map (locally, the unique metric projection), let $Y := g(X)$ and $P_{\text{marg}} := g_{\#}\mathcal{N}(\mu, \Sigma)$ as in (5). This section quantifies, in W_2 , the discrepancy between P_{marg} and a tangent–retraction surrogate. Given a linearization point $\tilde{\mu} \in \mathcal{M}$, write $T := T_{\tilde{\mu}}\mathcal{M}$ with orthogonal projector Π_T and define

$$\begin{aligned} \hat{g}(x) &:= \bar{R}(\Pi_T(x - \tilde{\mu})), \\ \hat{Y} &:= \hat{g}(X), \\ \hat{P}_{\text{marg}} &:= \mathcal{L}(\hat{Y}). \end{aligned} \quad (10)$$

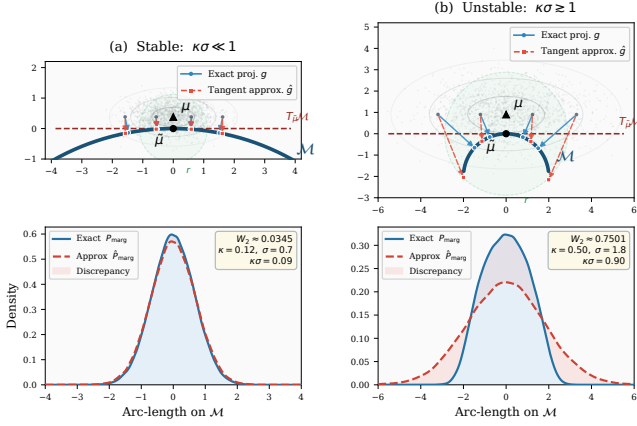


Fig. 1: W_2 stability of marginalizing a Gaussian onto a circular arc. Exact metric projection g vs. the tangent–retraction approximation \hat{g} .

where $\bar{R} : T \rightarrow \mathcal{M}$ is a measurable extension of a local retraction $R_{\tilde{\mu}} : B_T(r) \rightarrow \mathcal{M}$ outside $B_T(r)$, chosen so that the fourth moment in C_{tail} below is finite (for instance, by using a constant extension outside $B_T(r)$). The retraction satisfies the quadratic accuracy bound (4). The main estimate below separates a local second-order geometric error from a tail contribution outside the localization radius r .

Geometric locality: Assume $\text{reach}(\mathcal{M}) \geq \rho > 0$ and fix $r \in (0, \rho/2)$. Under this assumption, g coincides with the unique metric projection on the tube $\mathcal{T}_\rho(\mathcal{M})$. Assume a local curvature bound on $\mathcal{M} \cap B(\tilde{\mu}, 2r)$:

$$\sup_{y \in \mathcal{M} \cap B(\tilde{\mu}, 2r)} \|\Pi_y\|_{\text{op}} \leq \kappa. \quad (11)$$

Theorem III.1 (W_2 stability of marginalization under tangent–retraction). *There exists a constant $C_{\text{loc}} > 0$ (depending only on dimensionless tube/curvature margins, e.g. r/ρ and $r\kappa$, and on the ambient dimension) such that, with $A := \{\|X - \tilde{\mu}\| \leq r\}$ and $\varepsilon := \mathbb{P}(A^c)$,*

$$W_2(P_{\text{marg}}, \hat{P}_{\text{marg}}) \leq C_{\text{loc}}(\kappa + \kappa_R) \left(\mathbb{E}[\|X - \tilde{\mu}\|^4 \mathbf{1}_A] \right)^{1/2} + C_{\text{tail}} \varepsilon^{1/4}, \quad (12)$$

where

$$C_{\text{tail}} := \left(\mathbb{E}\|Y - \tilde{\mu}\|^4 \right)^{1/4} + \left(\mathbb{E}\|\hat{Y} - \tilde{\mu}\|^4 \right)^{1/4} < \infty.$$

Remark III.2 (Practical calibration of C_{loc}). C_{loc} depends only on local geometry, not on (μ, Σ) . It can be estimated by sampling $x_j \in B(\tilde{\mu}, r)$, computing the ratio $\|g(x_j) - R_{\tilde{\mu}}(\Pi_T(x_j - \tilde{\mu}))\| / ((\kappa + \kappa_R)\|x_j - \tilde{\mu}\|^2)$, and taking a high quantile with a safety factor.

Proof of Theorem III.1. We couple $Y = g(X)$ and $\hat{Y} = \hat{g}(X)$ through the same Gaussian input X , and we estimate $\mathbb{E}\|Y - \hat{Y}\|^2$ by separating a local region (where geometry is second-order accurate) from its complement. The deterministic part is a local comparison between metric projection and the tangent–retraction map.

Lemma III.3 (Local quadratic comparison of projection and tangent–retraction). *Under the geometric locality assumptions (Equation (11)), let $R_{\tilde{\mu}} : B_T(r) \rightarrow \mathcal{M}$ be a C^2 retraction with (4). Then there exists $C_{\text{loc}} > 0$ such that for every x with $\|x - \tilde{\mu}\| \leq r$,*

$$\|g(x) - R_{\tilde{\mu}}(\Pi_T(x - \tilde{\mu}))\| \leq C_{\text{loc}}(\kappa + \kappa_R)\|x - \tilde{\mu}\|^2. \quad (13)$$

Proof. Fix x with $d := \|x - \tilde{\mu}\| \leq r$, $y := g(x) \in \mathcal{M}$, and $v := \Pi_T(x - \tilde{\mu}) \in T$. Since $r < \rho$, the metric projection satisfies $\text{Lip}(g|_{\mathcal{T}_r}) \leq \rho/(\rho - r) \leq 2$, giving $\|y - \tilde{\mu}\| \leq 2d$. Standard C^2 graph estimates [19, 20] yield, for $z \in \mathcal{M} \cap B(\tilde{\mu}, 2r)$,

$$\|\Pi_{T^\perp}(z - \tilde{\mu})\| \leq \frac{C_{\text{ht}}\kappa}{2}\|z - \tilde{\mu}\|^2, \quad (14)$$

$$\|\Pi_{T_z\mathcal{M}} - \Pi_T\|_{\text{op}} \leq C_{\text{ang}}\kappa\|z - \tilde{\mu}\|. \quad (15)$$

Since $\Pi_{T_y\mathcal{M}}(x - y) = 0$, applying (15) at $z = y$ gives $\|v - \Pi_T(y - \tilde{\mu})\| \leq 3C_{\text{ang}}\kappa d^2$, and (14) gives $\|\Pi_{T^\perp}(y - \tilde{\mu})\| \leq 2C_{\text{ht}}\kappa d^2$. Hence $\|y - (\tilde{\mu} + v)\| \leq C_{\text{proj}}\kappa d^2$ with $C_{\text{proj}} := 2C_{\text{ht}} + 3C_{\text{ang}}$, and the retraction bound (4) completes the triangle inequality to (13). \square

Returning to the random setting, the shared-input coupling and (2) give

$$W_2(\mathcal{L}(Y), \mathcal{L}(\hat{Y})) \leq \left(\mathbb{E}\|Y - \hat{Y}\|^2 \right)^{1/2}. \quad (16)$$

Let $A := \{\|X - \tilde{\mu}\| \leq r\}$. Splitting the second moment over A and A^c ,

$$\mathbb{E}\|Y - \hat{Y}\|^2 := \mathbb{E}[\|Y - \hat{Y}\|^2 \mathbf{1}_A] + \mathbb{E}[\|Y - \hat{Y}\|^2 \mathbf{1}_{A^c}]. \quad (17)$$

On A , Lemma III.3 yields

$$\|Y - \hat{Y}\| \leq C_{\text{loc}}(\kappa + \kappa_R)\|X - \tilde{\mu}\|^2,$$

therefore

$$\left(\mathbb{E}[\|Y - \hat{Y}\|^2 \mathbf{1}_A] \right)^{1/2} \leq C_{\text{loc}}(\kappa + \kappa_R) \times \left(\mathbb{E}[\|X - \tilde{\mu}\|^4 \mathbf{1}_A] \right)^{1/2}. \quad (18)$$

On A^c , setting $Z := \|Y - \tilde{\mu}\| + \|\hat{Y} - \tilde{\mu}\|$ and applying Hölder ($L^4/L^{4/3}$) followed by Minkowski gives $(\mathbb{E}[\|Y - \hat{Y}\|^2 \mathbf{1}_{A^c}])^{1/2} \leq C_{\text{tail}} \varepsilon^{1/4}$. Combining with (16), (17), and (18) yields (12). \square

Gaussian specialization: Set $\delta := \mu - \tilde{\mu}$ and write $X - \tilde{\mu} = \delta + \xi$ with $\xi \sim \mathcal{N}(0, \Sigma)$. Then the untruncated fourth moment in (12) has the closed form

$$\mathbb{E}\|X - \tilde{\mu}\|^4 = \|\delta\|^4 + 2\|\delta\|^2 \text{tr} \Sigma + 4\delta^\top \Sigma \delta + (\text{tr} \Sigma)^2 + 2\|\Sigma\|_F^2. \quad (19)$$

On $A := \{\|X - \tilde{\mu}\| \leq r\}$, the localized fourth moment satisfies $\mathbb{E}[\|X - \tilde{\mu}\|^4 \mathbf{1}_A] \leq r^4$ and can be sharpened via the CDF of $\|X - \tilde{\mu}\|^2$.

For the tail probability $\varepsilon := \mathbb{P}(A^c)$, let $\lambda_{\text{max}} := \|\Sigma\|_{\text{op}}$ and $Z \sim \mathcal{N}(0, I_n)$. Using $\mathbb{P}(\|Z\| \geq \sqrt{n} + t) \leq e^{-t^2/2}$ [21] yields, for any $r > \|\delta\|$,

$$\varepsilon = \mathbb{P}(\|X - \tilde{\mu}\| > r) \leq \exp\left(-\frac{1}{2}\left(\frac{r - \|\delta\|}{\sqrt{\lambda_{\text{max}}}} - \sqrt{n}\right)_+^2\right). \quad (20)$$

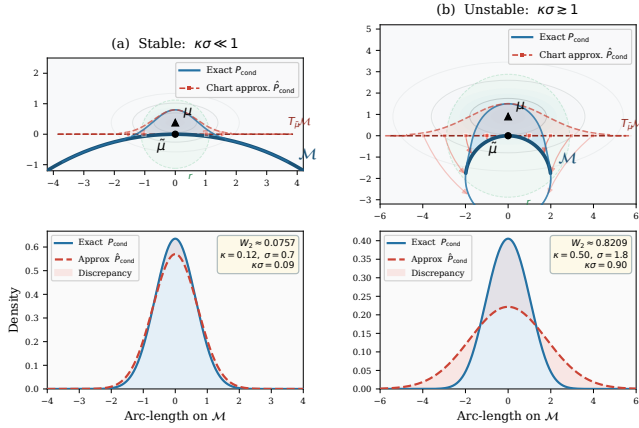


Fig. 2: W_2 stability of conditioning a Gaussian onto a circular arc. Surface-measure conditioning vs. a tangent-plane chart approximation.

Choosing $r = \|\delta\| + \sqrt{\lambda_{\max}}(\sqrt{n} + t)$ gives $\varepsilon \leq e^{-t^2/2}$. The constant C_{tail} can be made fully explicit for a nearest-point g and a bounded or at-most-quadratic extension \tilde{R} : Lipschitz projection inside the tube ($\text{Lip}(g) \leq \rho/(\rho - r)$), nearest-point control outside it, and retraction accuracy (4) bound the relevant fourth-moment terms by Gaussian moments of $\|X - \tilde{\mu}\|$, yielding a computable criterion from (μ, Σ) and $(\rho, \kappa, \kappa_R, r)$.

Interpretation and numerical illustration: Equation (12) decomposes the error into a local geometric term and a tail-leakage term. Inside $A = \{\|X - \tilde{\mu}\| \leq r\}$, the mismatch between g and \hat{g} is second order, scaling as $(\kappa + \kappa_R)\|X - \tilde{\mu}\|^2$ (Lemma III.3). For Gaussian inputs, the effective spread scale is $\|\delta\| + \sqrt{\lambda_{\max}}\sqrt{n}$, so the local term is roughly $(\kappa + \kappa_R)(\|\delta\| + \sqrt{\lambda_{\max}}\sqrt{n})^2$. The tail term is controlled by $\varepsilon = \mathbb{P}(\|X - \tilde{\mu}\| > r)$ and decays exponentially once $r \gtrsim \|\delta\| + \sqrt{\lambda_{\max}}(\sqrt{n} + t)$, but can dominate when reach forces small r . Hence, r must balance probability-mass coverage against local geometric validity. Figure 1 supports this prediction: in local regimes, the exact and approximate laws nearly coincide. Beyond the transition, linearization becomes miscalibrated and typically overconfident. The spectral scale $\|\Sigma\|_{\text{op}}$ is a worst-case proxy for how much probability mass can leave the local tube. In the projection geometries tested below, uncertainty with a large normal component is the dominant failure mode because it stresses curvature and reach most directly. The height and angle estimates (14)–(15) still control general local displacements, so tangent-dominant uncertainty is covered by the theorem but can make the spectral bound conservative (confirmed in Section V).

IV. W_2 STABILITY FOR GAUSSIAN CONDITIONING

Unlike marginalization, conditioning depends on density shape on \mathcal{M} , not just mass transport. We therefore replace the direct coupling of Section III with likelihood-ratio and total-variation arguments. Let $\mathcal{M} \subset \mathbb{R}^n$ be a C^2 embedded submanifold of dimension d and $X \sim \mathcal{N}(\mu, \Sigma)$ with density $\varphi_{\mu, \Sigma}$. Assume the surface-measure restriction has $0 < Z_{\mathcal{M}} < \infty$ and finite second moment. This section quantifies, in W_2 ,

the discrepancy between the exact conditioned law P_{cond} from (6) (with $\varphi = \varphi_{\mu, \Sigma}$) and an approximation that first conditions on $T_{\tilde{\mu}}\mathcal{M}$ and then maps back to \mathcal{M} through a local chart.

Tangent-plane reference law: Fix $\tilde{\mu} \in \mathcal{M}$ and let $T := T_{\tilde{\mu}}\mathcal{M}$ as in Section III. Let $N \in \mathbb{R}^{n \times d}$ have orthonormal columns spanning T and define the affine parametrization $x_{\text{lin}}(v) = \tilde{\mu} + Nv$ for $v \in \mathbb{R}^d$. Let $\Omega := \Sigma^{-1}$ denote the precision matrix, and recall $\delta = \mu - \tilde{\mu}$ from Section III. Define the probability measure Q_T on \mathbb{R}^d by

$$dQ_T(v) := \frac{\varphi_{\mu, \Sigma}(\tilde{\mu} + Nv)}{Z_T} dv, \quad (21)$$

$$Z_T := \int_{\mathbb{R}^d} \varphi_{\mu, \Sigma}(\tilde{\mu} + Nv) dv \in (0, \infty).$$

Equivalently, $Q_T = \mathcal{N}(m_T, \Sigma_T)$ with

$$\Sigma_T = (N^\top \Omega N)^{-1}, \quad m_T = \Sigma_T N^\top \Omega \delta. \quad (22)$$

Chart model and approximation: Fix $r > 0$ and write $B_r := \{v \in \mathbb{R}^d : |v| \leq r\}$. Assume $\Psi : B_r \rightarrow \mathcal{M}$ is a C^2 embedding onto $\mathcal{M}_r := \Psi(B_r)$ with $\Psi(0) = \tilde{\mu}$, $D\Psi(0) = N$, and $\text{Lip}(\Psi) \leq L_\Psi$ on B_r . Assume the second-order residual bound

$$\|\Psi(v) - (\tilde{\mu} + Nv)\| \leq \frac{\kappa_\Psi}{2} |v|^2, \quad v \in B_r, \quad (23)$$

and a quadratic control on the Jacobian factor $J(v)$ defined by $d\text{Vol}_{\mathcal{M}}(\Psi(v)) = J(v) dv$:

$$|\log J(v)| \leq \frac{\kappa_J}{2} |v|^2, \quad v \in B_r, \quad (24)$$

Let $\bar{\Psi} : \mathbb{R}^d \rightarrow \mathcal{M}$ be a measurable extension of Ψ such that $\bar{\Psi}(v) \in \mathcal{M}_r$ iff $v \in B_r$ and $\tau_{\bar{\Psi}}(r) < \infty$ (e.g., when $\mathcal{M} \setminus \mathcal{M}_r \neq \emptyset$, map $v \notin B_r$ to any fixed point in $\mathcal{M} \setminus \mathcal{M}_r$), and define the approximate conditioned law

$$\hat{P}_{\text{cond}} := \bar{\Psi}_\# Q_T. \quad (25)$$

Tail quantities: Define

$$\varepsilon_P := P_{\text{cond}}(\mathcal{M} \setminus \mathcal{M}_r), \quad \varepsilon_Q := Q_T(\mathbb{R}^d \setminus B_r), \quad (26)$$

and the corresponding tail second moments (w.r.t. $\tilde{\mu}$)

$$\tau_P(r) := \left(\mathbb{E}[\|Y - \tilde{\mu}\|^2 \mathbf{1}_{\{Y \notin \mathcal{M}_r\}}] \right)^{1/2}, \quad (Y \sim P_{\text{cond}}),$$

$$\tau_{\hat{P}}(r) := \left(\mathbb{E}[\|\hat{Y} - \tilde{\mu}\|^2 \mathbf{1}_{\{\hat{Y} \notin \mathcal{M}_r\}}] \right)^{1/2}, \quad (\hat{Y} \sim \hat{P}_{\text{cond}}). \quad (27)$$

Define the curvature/volume mismatch exponent

$$\eta_r := \frac{\|\Omega\| \kappa_\Psi}{2} (\|\delta\| + r) r^2 + \frac{\|\Omega\| \kappa_\Psi^2}{8} r^4 + \frac{\kappa_J}{2} r^2. \quad (28)$$

Theorem IV.1 (W_2 stability of surface-measure conditioning under chart linearization). *Under the assumptions above,*

$$W_2(P_{\text{cond}}, \hat{P}_{\text{cond}}) \leq \tau_P(r) + \tau_{\hat{P}}(r) + L_\Psi r (\sqrt{\varepsilon_P} + \sqrt{\varepsilon_Q}) + 2L_\Psi r \sqrt{\tanh(\eta_r)}. \quad (29)$$

Lemma IV.2 (Truncation bound). *Let P be a probability measure on a subset of \mathbb{R}^m with finite second moment. Let A*

be measurable with $P(A) = 1 - \varepsilon \in (0, 1]$, and let $P(\cdot | A)$ be the conditional law. Fix any $x_0 \in A$ and define $R_A := \sup_{x \in A} \|x - x_0\|$ (possibly $+\infty$). Then

$$W_2(P, P(\cdot | A)) \leq \left(\mathbb{E}[\|X - x_0\|^2 \mathbf{1}_{A^c}] \right)^{1/2} + R_A \sqrt{\varepsilon}, \quad (X \sim P). \quad (30)$$

Proof. Define the auxiliary measure $\tilde{P} := (1 - \varepsilon)P(\cdot | A) + \varepsilon \delta_{x_0}$. Couple P with \tilde{P} by keeping the mass on A fixed and sending all A^c mass to x_0 . By (2), this gives

$$W_2(P, \tilde{P}) \leq \left(\mathbb{E}[\|X - x_0\|^2 \mathbf{1}_{A^c}] \right)^{1/2}.$$

Next, couple \tilde{P} to $P(\cdot | A)$ by moving the extra point mass $\varepsilon \delta_{x_0}$ into A according to $P(\cdot | A)$, with cost at most $R_A \sqrt{\varepsilon}$. The claim follows by the triangle inequality. \square

Lemma IV.3 (Diameter-TV control of W_2 on bounded support). *Let p, q be probability measures supported on a set $S \subset \mathbb{R}^d$ with $\text{diam}(S) := \sup_{u, v \in S} \|u - v\| < \infty$. Then*

$$W_2(p, q) \leq \text{diam}(S) \sqrt{\text{TV}(p, q)}, \quad \text{TV}(p, q) := \frac{1}{2} \int |dp - dq|. \quad (31)$$

Proof. Let γ be a maximal coupling of (p, q) so that $\gamma\{(U, V) : U \neq V\} = \text{TV}(p, q)$ [22]. On $\{U = V\}$ the cost is 0, and on $\{U \neq V\}$ we have $\|U - V\| \leq \text{diam}(S)$. Thus $\mathbb{E}_\gamma \|U - V\|^2 \leq \text{diam}(S)^2 \text{TV}(p, q)$, and the claim follows by infimizing over couplings. \square

Lemma IV.4 (TV control from a likelihood-ratio bound). *Let p, q be probability measures with $p \ll q$ and*

$$\frac{dp}{dq} \in [\Lambda^{-1}, \Lambda] \quad q\text{-a.e.},$$

for some $\Lambda \geq 1$. Then

$$\text{TV}(p, q) \leq \frac{\Lambda - 1}{\Lambda + 1}.$$

Proof. Write $h := dp/dq \in [\Lambda^{-1}, \Lambda]$, so $\text{TV}(p, q) = \frac{1}{2} \mathbb{E}_q[|h - 1|]$ with $\mathbb{E}_q[h] = 1$. Since $x \mapsto |x - 1|$ is convex on $[\Lambda^{-1}, \Lambda]$, linear interpolation gives $\mathbb{E}_q[|h - 1|] \leq 2(\Lambda - 1)/(\Lambda + 1)$, hence the result. \square

Proof of Theorem IV.1. Recall P_{cond} from (6), Q_T from (21), and $\hat{P}_{\text{cond}} = \bar{\Psi}_\# Q_T$ from (25). Let $\mathcal{M}_r = \Psi(B_r)$, and define truncations

$$P_{\text{cond}}^{(r)} := P_{\text{cond}}(\cdot | \mathcal{M}_r), \quad \hat{P}_{\text{cond}}^{(r)} := \hat{P}_{\text{cond}}(\cdot | \mathcal{M}_r).$$

We first separate tail and interior contributions. By the triangle inequality,

$$W_2(P_{\text{cond}}, \hat{P}_{\text{cond}}) \leq W_2(P_{\text{cond}}, P_{\text{cond}}^{(r)}) + W_2(P_{\text{cond}}^{(r)}, \hat{P}_{\text{cond}}^{(r)}) + W_2(\hat{P}_{\text{cond}}^{(r)}, \hat{P}_{\text{cond}}). \quad (32)$$

Lemma IV.2 with $A = \mathcal{M}_r$, $x_0 = \tilde{\mu}$, and $\sup_{x \in \mathcal{M}_r} \|x - \tilde{\mu}\| \leq L_\Psi r$ bounds the two outer (tail) terms:

$$W_2(P_{\text{cond}}, P_{\text{cond}}^{(r)}) \leq \tau_P(r) + L_\Psi r \sqrt{\varepsilon_P}, \quad (33)$$

$$W_2(\hat{P}_{\text{cond}}^{(r)}, \hat{P}_{\text{cond}}) \leq \tau_{\hat{P}}(r) + L_{\Psi} r \sqrt{\varepsilon_Q}. \quad (34)$$

For the interior, pull both truncated laws back to B_r via the bijection Ψ . Define unnormalized densities $\tilde{p}(v) := \varphi_{\mu, \Sigma}(\Psi(v))J(v)$ and $\tilde{q}(v) := \varphi_{\mu, \Sigma}(\tilde{\mu} + Nv)$, and let $p_r := \tilde{p}/\int_{B_r} \tilde{p}$, $q_r := \tilde{q}/\int_{B_r} \tilde{q}$. Then $P_{\text{cond}}^{(r)} = \Psi_\# p_r$ and $\hat{P}_{\text{cond}}^{(r)} = \Psi_\# q_r$. By (3) and Lemma IV.3 ($\text{diam}(B_r) \leq 2r$),

$$W_2(P_{\text{cond}}^{(r)}, \hat{P}_{\text{cond}}^{(r)}) \leq 2L_\Psi r \sqrt{\text{TV}(p_r, q_r)}.$$

Write $e(v) := \Psi(v) - (\tilde{\mu} + Nv)$. By (23), $\|e(v)\| \leq \frac{\kappa_\Psi}{2} r^2$ on B_r . Expanding the log-density difference and applying (24) gives $|\log \tilde{p}(v) - \log \tilde{q}(v)| \leq \eta_r$ on B_r . After normalization, $p_r/q_r \in [e^{-2\eta_r}, e^{2\eta_r}]$, and Lemma IV.4 yields $\text{TV}(p_r, q_r) \leq \tanh(\eta_r)$. Inserting the tail and interior bounds into (32) gives (29). \square

Gaussian specialization: For $Q_T = \mathcal{N}(m_T, \Sigma_T)$ from (22), the tail $\varepsilon_Q := Q_T(\mathbb{R}^d \setminus B_r)$ is bounded by Gaussian concentration as in (20) with $(\delta, \Sigma) \rightarrow (m_T, \Sigma_T)$. If the extension satisfies $\|\bar{\Psi}(v) - \tilde{\mu}\| \leq L_{\text{ext}}(1 + \|v\|)$ on $\mathbb{R}^d \setminus B_r$, then Cauchy-Schwarz gives $\tau_{\hat{P}}(r) \leq L_{\text{ext}}(\mathbb{E}(1 + \|V\|)^4)^{1/4} \varepsilon_Q^{1/4}$; for a constant tail extension to z_0 , one may instead use $\tau_{\hat{P}}(r) \leq \|z_0 - \tilde{\mu}\| \sqrt{\varepsilon_Q}$. The Gaussian fourth moment appearing here has the same form as (19). The remaining $(\varepsilon_P, \tau_P(r))$ quantify the true conditioned mass outside \mathcal{M}_r .

Interpretation and numerical illustration: Equation (29) splits conditioning error into tail/truncation penalties ($\tau_P, \tau_{\hat{P}}, \varepsilon_P, \varepsilon_Q$ terms) and interior chart distortion $2L_\Psi r \sqrt{\tanh(\eta_r)}$, where η_r combines second-order chart residual and Jacobian distortion weighted by $\|\Omega\|$. For affine manifolds ($\kappa_\Psi = \kappa_J = 0$), $\eta_r = 0$ and only truncation remains. In robotics, enforcing hard constraints (e.g. unit-quaternion normalization, contact membership) is conditioning, and η_r quantifies how constraint curvature and prior precision jointly warp the tangent approximation. When $\eta_r \ll 1$, a single tangent chart is faithful, but as η_r grows the chart distortion dominates and manifests as miscalibrated credible regions on \mathcal{M} . Figure 2 illustrates this transition: near-local regimes show close agreement, whereas larger spread introduces mode/variance mismatch and then tail-dominated failure.

V. NUMERICAL EXPERIMENTS

A. 2-D circle benchmark

Goals and setup: We consider $\mathcal{M} = \{x \in \mathbb{R}^2 : \|x\| = R\}$ with curvature $\kappa = 1/R$, reach $\rho = R$, and $X \sim \mathcal{N}(\mu, \Sigma)$ where $\mu = (R + \delta, 0)$. The baseline uses isotropic covariance $\Sigma = \sigma^2 I_2$ with $\delta = 0.2$. We then add two stress tests to assess robustness: (i) anisotropic covariance, $\Sigma = \text{diag}(\sigma_n^2, \sigma_t^2)$ in the normal/tangential frame, and (ii) offset sweeps in δ/R . These tests probe the computable diagnostics in Theorem III.1, especially the roles of $\sqrt{\|\Sigma\|_{\text{op}}}$ and the tail-leakage term ε . For marginalization, the exact map is $g(x) = Rx/\|x\|$, and the approximation is tangent projection plus normalization at

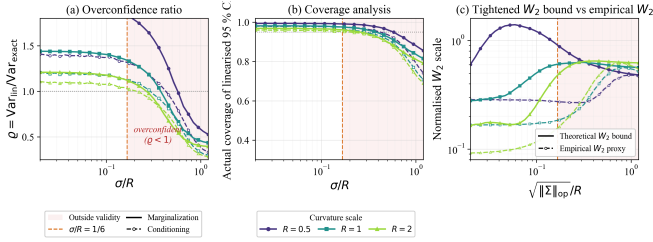


Fig. 3: Circle sweep ($\delta = 0.2$) over σ/R : (a) variance ratio $\rho = \text{Var}_{\text{lin}}/\text{Var}_{\text{exact}}$, (b) realized 95% coverage, and (c) normalized diagnostics on $\sqrt{\|\Sigma\|_{\text{op}}}/R$: tightened theoretical W_2 bound (data-calibrated C_{tail} with strict upper-envelope safeguard) and empirical W_2 proxy. Dashed line marks $\sigma/R = 1/6$. Colors indicate $R \in \{0.5, 1, 2\}$.

$\tilde{\mu} = g(\mu) = (R, 0)$. For conditioning, we compare surface-measure conditioning on \mathcal{M} against tangent-line conditioning followed by retraction.

Quantitative sweep: Figure 3 sweeps $\sigma/R \in [0.02, 1.2]$ for $R \in \{0.5, 1, 2\}$ and reports (i) variance ratio $\rho = \text{Var}_{\text{lin}}(\theta)/\text{Var}_{\text{exact}}(\theta)$, (ii) coverage of a nominal 95% interval, and (iii) normalized theoretical/empirical W_2 diagnostics for marginalization. Panel (a) shows ρ beginning to drop after the $\sigma/R = 1/6$ locality marker and crossing below 1 only at larger spread. Panel (b) shows corresponding coverage degradation outside the local regime. Panel (c) uses $\sqrt{\|\Sigma\|_{\text{op}}}/R$ and compares empirical W_2 proxies against tightened theoretical W_2 bounds with data-calibrated C_{tail} (90% quantile pre-fit with a strict upper-envelope safeguard), so the bound remains above the empirical proxy while preserving the failure-onset trend.

Anisotropic Σ and offset sweeps: Figure 4 extends the circle benchmark along two complementary axes. Panel (a) varies anisotropy $\eta := \sigma_n/\sigma_t \in \{0.5, 1, 2, 4\}$ and replots calibration against the spectral scale $\sqrt{\|\Sigma\|_{\text{op}}}/R$. The transition remains aligned across anisotropy levels, supporting $\|\Sigma\|_{\text{op}}$ as an effective diagnostic variable in the bound. Panels (b)–(c) fix anisotropy and sweep δ/R : as offset increases, the tail proxy ε rises rapidly and coverage degrades even at fixed curvature/noise scale, revealing a second failure axis beyond curvature-only effects. This behavior matches the decomposition in Theorem III.1, where local distortion and nonlocal leakage contribute separately. Formally, $\|\delta\|$ enters both (19) and (20), confirming mean offset as a failure axis independent of $\sqrt{\|\Sigma\|_{\text{op}}}/\rho$.

Conditioning comparison: Applying the same circle benchmark to conditioning (Figure 2), the tangent-chart approximation breaks down *before* its marginalization counterpart: the conditioning variance ratio approaches unity and crosses into the below-unity, overconfident regime at a smaller σ/R than marginalization (≈ 0.30 vs. ≈ 0.38), consistent with Theorem IV.1 where $\kappa_{\mathcal{J}}$ and $\|\Omega\|_{\kappa_{\Psi}}$ jointly amplify chart distortion beyond what curvature alone causes for projection. Already at $\sigma/R \approx 1/6$, conditioning retains less overconfidence headroom than marginalization (variance ratio ≈ 1.13 vs. ≈ 1.34). At $\sigma/R \approx 0.5$ the exact conditioned density exhibits a qualitatively different concentration pattern—different kurtosis and tail weight—compared to the tangent-

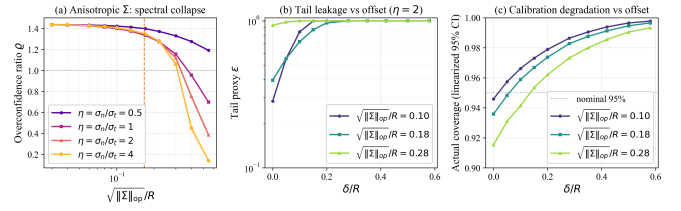


Fig. 4: Circle generality stress tests: (a) anisotropic sweep ($\eta = \sigma_n/\sigma_t$) versus $\sqrt{\|\Sigma\|_{\text{op}}}/R$, (b) tail proxy ε versus offset δ/R , and (c) coverage degradation versus δ/R .

TABLE I: Quantitative covariance metrics for planar pushing at timesteps

k	$\text{tr}(\Sigma_{xy})$		$\lambda_{\max}(\Sigma_{xy})$		Red. (%)	$\ \Delta\Sigma_{xy}\ _F$
	Unc.	Con.	Unc.	Con.		
1	0.0018	0.0009	0.0009	0.0009	50.5	0.0009
13	0.0234	0.0105	0.0117	0.0105	55.3	0.0118
25	0.0450	0.0190	0.0225	0.0190	57.8	0.0228
37	0.0666	0.0278	0.0333	0.0278	58.2	0.0337
49	0.0882	0.0377	0.0441	0.0377	57.3	0.0446

chart approximation, illustrating density-shape artifacts that W_2 may underestimate (see Section VI).

B. Planar pushing: diagnostics in a contact-rich task

Setup and covariance models: We use the standard 2-D planar-pushing benchmark from constrained GTSAM/InCOpt to evaluate covariance extraction under hard contact constraints [2, 3]. A rectangular box state $x_k = (p_{x,k}, p_{y,k}, \theta_k) \in \mathbb{R}^2 \times \mathbb{S}^1$ is pushed by a circular probe whose center follows a known deterministic path. The probe is assumed to remain in contact with the box boundary at every step, encoded as a per-pose contact factor $c_k(x_k) = 0$. Odometry provides relative-pose measurements with wrapped-angle noise, $u_k = x_{k+1} - x_k + \varepsilon_k$, $\varepsilon_k \sim \mathcal{N}(0, Q)$, $Q = \text{diag}(0.03^2, 0.03^2, 0.01^2)$. We use $r_p = 0.1$ m, $(w, h) = (0.2, 1.0)$ m, and $n_{\text{steps}} = 50$. The constrained mean is obtained from constrained least squares:

$$\min_{x_{1:n}} \sum_{k=0}^{n-1} \|r_k(x)\|_{Q^{-1}}^2 \quad \text{s.t.} \quad c_k(x_k) = 0, \quad \forall k,$$

with $r_k(x) := x_{k+1} - (x_k + u_k)$. Linearizing about the optimized trajectory, we form the (unconstrained) Gauss–Newton information $F \approx H^\top W^{-1} H$ with $W = \text{blkdiag}(Q, \dots, Q)$, giving $\Sigma_{\text{unc}} = F^{-1}$, and compute the constrained covariance by conditioning onto the linearized contact constraints: $\Sigma_{\text{con}} = N(N^\top F N)^{-1} N^\top$, where $N \in \text{null}(S^\top)$ spans the tangent directions of the constraint manifold.

Aggregate covariance reduction: Across 49 optimized timesteps, equality constraints are satisfied to numerical precision. Table I reports representative timesteps: the constrained xy -marginal covariance trace is reduced by 50.5% at $k = 1$ and 57.3% at $k = 49$, with a peak reduction of 58.2% at $k = 37$. These values establish a trajectory-level baseline before the Monte Carlo calibration diagnostics.

Trajectory-wide diagnostics: To move beyond single-pose checks, we evaluate diagnostics at every timestep. Let $c_k(x) = 0$ be the contact constraint at step k , linearized at

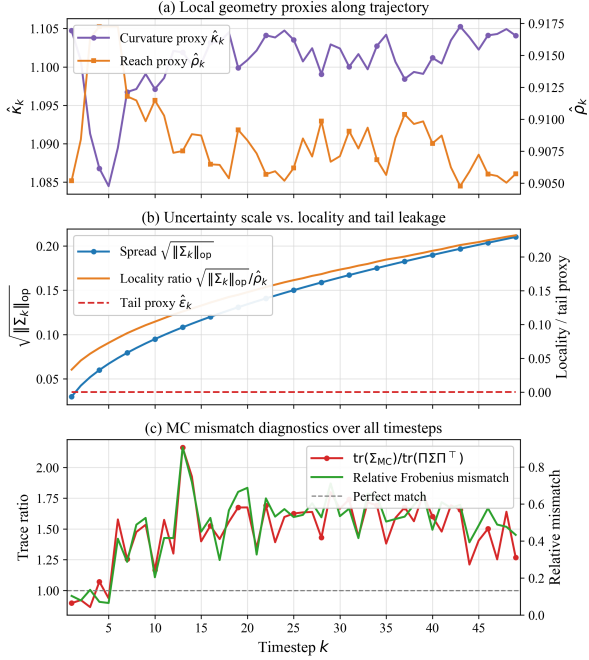


Fig. 5: Trajectory-wide planar-pushing diagnostics: (a) curvature/reach proxies ($\hat{\kappa}_k, \hat{\rho}_k$), (b) spread s_k and locality indicator $s_k/\hat{\rho}_k$, (c) Monte Carlo mismatch ($\varrho_k^{\text{MC}}, \Delta_k$).

\hat{x}_k . With N_k spanning $\text{null}(\nabla c_k(\hat{x}_k)^\top)$, we define

$$\hat{\kappa}_k := \frac{\|N_k^\top \nabla^2 c_k(\hat{x}_k) N_k\|_{\text{op}}}{\|\nabla c_k(\hat{x}_k)\|}, \quad \hat{\rho}_k := \frac{1}{\max(\hat{\kappa}_k, \epsilon_\kappa)}, \quad (35)$$

as curvature/reach proxies ($\epsilon_\kappa = 10^{-8}$ for numerical stability), and the uncertainty spread

$$s_k := \sqrt{\|\Sigma_{\text{unc},k}\|_{\text{op}}}. \quad (36)$$

At each k , we compare tangent-plane covariance $\Sigma_{\text{lin},k} := \Pi_k \Sigma_{\text{unc},k} \Pi_k^\top$ against Monte Carlo covariance $\Sigma_{\text{MC},k}$ after exact nonlinear projection, via

$$\varrho_k^{\text{MC}} := \frac{\text{tr}(\Sigma_{\text{MC},xy,k})}{\text{tr}(\Sigma_{\text{lin},xy,k})}, \quad \Delta_k := \frac{\|\Sigma_{\text{MC},xy,k} - \Sigma_{\text{lin},xy,k}\|_F}{\|\Sigma_{\text{lin},xy,k}\|_F}. \quad (37)$$

Figure 5 shows a non-uniform failure profile over time. Larger mismatch co-occurs with larger locality-pressure indicators ($s_k/\hat{\rho}_k$), consistent with the tail-leakage interpretation in Theorem III.1. The largest mismatch occurs at $k = 13$ ($\varrho_{13}^{\text{MC}} = 2.162$, locality index $s_{13}/\hat{\rho}_{13} = 0.119$). The median trajectory-wide mismatch is $\text{median}(\varrho_k^{\text{MC}}) = 1.557$ with median relative Frobenius discrepancy $\text{median}(\Delta_k) = 0.525$.

Directional uncertainty stress test: Isotropic scaling $\Sigma \mapsto \alpha^2 \Sigma$ obscures direction-specific failures. At the terminal pose k^* , with local unit normal \hat{n} , define $A(\alpha_n, \alpha_t) := \alpha_t(I - \hat{n}\hat{n}^\top) + \alpha_n\hat{n}\hat{n}^\top$ and $\Sigma(\alpha_n, \alpha_t) := A\Sigma_{\text{unc},k^*}A^\top$. We compare isotropic (α, α), normal-only ($\alpha, 1$), and tangential-only ($1, \alpha$) sweeps. Figure 6 shows a clear asymmetry for $\alpha \geq 1$: normal-direction inflation causes the largest calibration and covariance mismatch. This normal-tangent asymmetry provides experimental confirmation of the mechanism in Theorem III.1: because $\|\Sigma\|_{\text{op}}$ captures the worst-case (normal)

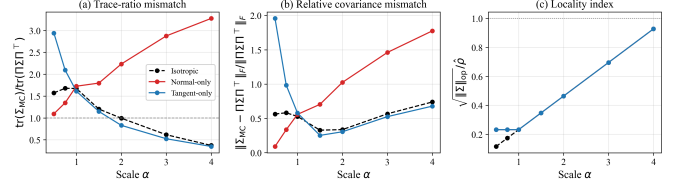


Fig. 6: Directional scaling at the terminal planar-pushing pose: isotropic, normal-only, and tangential-only covariance inflation.

spread, the bound tightens when the dominant eigenvalue aligns with the constraint normal, while remaining safely conservative for tangent-dominant uncertainty.

VI. DISCUSSION

Practical validity test for robotics estimation: The bounds give a runtime calibration gate for factor-graph pipelines. At each linearization point $\tilde{\mu}$, compute $k_\rho := \sqrt{\|\Sigma\|_{\text{op}}/\rho}$ and $s_\delta := \|\delta\|/\rho$ from the marginal covariance, local reach/curvature, and linearization offset. Curvature is analytic for S^3 , $SO(3)$, and $SE(3)$, or can be approximated from the constraint Jacobian/Hessian as in Section V-B. If $k_\rho \lesssim 1/6$ and $s_\delta \ll 1$, the tangent approximation is reliable; otherwise the decomposition suggests iterated relinearization for large k_ρ with small s_δ [23], immediate relinearization for large s_δ (e.g. after a loop closure), and multi-chart [24, 25] or particle [26, 27] methods when both are large. For conditioning, $\eta_r \ll 1$ is an additional guard against chart-distortion artifacts that W_2 may underestimate. The cost is one dominant-eigenvalue query plus a curvature lookup per variable; in GTSAM/iSAM2-style solvers, the covariance is available from the Bayes tree and curvature from analytic formulas or the constraint Hessian. Unlike chi-squared innovation tests, which detect residual inconsistency after measurement incorporation [1], these diagnostics predict linearization failure before the update and enable preemptive method switching.

W_2 scope and conditioning asymmetry: Because W_2 measures mass displacement rather than density shape, similar bounds for marginalization and conditioning do not imply equal robustness. Conditioning is more delicate: normalization constants such as Z_T^{-1} in (21) can amplify shape errors that W_2 does not penalize. For example, conditioning a Gaussian onto S^3 at moderate k_ρ may produce a narrow spherical cap with angular variance different from the tangent-Gaussian prediction, while W_2 remains moderate because the supports and centroids are close. Projection-based marginalization is less sensitive to this artifact because the projection map fixes the support before normalization, making W_2 a more faithful calibration proxy there. Conditioning should therefore be supplemented with coverage or KL checks when $k_\rho \gtrsim 0.1$.

Concrete regime examples: For unit-quaternion orientation on S^3 ($\kappa = 1, \rho = 1$), $k_\rho = \sqrt{\|\Sigma\|_{\text{op}}}$: IMU-grade uncertainty ($\lesssim 0.03$) is well below $1/6$, whereas prolonged dead reckoning ($\gtrsim 0.17$) exceeds it. For planar contact with $R_c \approx 0.1$ m, the threshold $\sqrt{\|\Sigma\|_{\text{op}}} \lesssim R_c/6 \approx 17$ mm is compatible with calibrated sensors but can be violated

by process-noise accumulation, as in Section V-B. Loop-closure drift gives the complementary offset trigger: $\sim 1\%$ drift implies $\|\delta\| \approx 0.5$ m after 50 m, far beyond the locality radius. For SE(3) with small rotation–translation cross-covariance [1], rotational uncertainty follows the chosen SO(3) or unit-quaternion embedding constants, translational constraints inherit $k_\rho = \sqrt{\|\Sigma_{\text{pos}}\|_{\text{op}}}/R_c$, and the leading-order diagnostic is the maximum of both.

Interaction between offset and anisotropy: In incremental solvers, $\|\delta\|$ and k_ρ often grow together because state lag and covariance growth accumulate simultaneously. When the dominant eigenvector of Σ aligns with the offset, the cross-term $4\delta^\top \Sigma \delta$ in (19) amplifies the local bound; if the offset is orthogonal to the dominant spread, only the additive $\|\delta\|^4$ term remains. The anisotropic circle experiments confirm that coverage degrades fastest when k_ρ and s_δ are large in the same direction.

Relation to nonlinear filtering methods: The same decomposition clarifies what different filters improve. Iterated Kalman filtering [23] reduces s_δ by re-evaluating at posterior modes, while invariant [11] and equivariant [12] filters exploit symmetry to reduce effective curvature on groups such as SO(3). Thus k_ρ and s_δ act as post-hoc certificates for the tangent approximation. If they remain above threshold after filtering, multi-chart or particle methods are warranted regardless of filter type.

Limitations: The constants are conservative (general coupling/concentration inequalities rather than manifold-specific transport). Specialized transport constructions, such as geodesic couplings on Lie groups, may tighten the constants and reduce the theory–experiment gap in Section V. The bounds are also per-variable and single-step, whereas coupled robotics constraints may compound tangent-approximation errors across variables and long-horizon cascades may require joint diagnostics. The analysis assumes C^2 manifolds with positive reach; piecewise-smooth contact manifolds, joint multi-variable diagnostics, and non-Gaussian priors remain future work.

VII. CONCLUSION

We derived explicit non-asymptotic W_2 stability bounds for tangent-linearized Gaussian marginalization and conditioning on smooth manifolds, decomposing error into local geometric distortion and tail leakage. For Gaussian inputs, the bounds yield closed-form diagnostics from (μ, Σ) and local curvature/reach, confirmed by circle and planar-pushing benchmarks that locate the calibration transition at $k_\rho \approx 1/6$ with normal-direction uncertainty as the dominant failure mode. A structural asymmetry emerges: conditioning degrades faster than marginalization because Z_T^{-1} amplifies density-shape distortions invisible to W_2 , while the mean-offset diagnostic s_δ provides a complementary escalation trigger for factor-graph solvers to adaptively switch between relinearization, multi-chart, and particle methods. Future extensions include piecewise-smooth geometries, joint multi-variable diagnostics, and non-Gaussian priors.

ACKNOWLEDGMENT

This work was supported by Deep-Tech TIPS funded by the Ministry of SMEs and Startups.

REFERENCES

- [1] T. D. Barfoot, *State estimation for robotics*. Cambridge University Press, 2024.
- [2] M. Qadri, P. Sodhi, J. G. Mangelson, F. Dellaert, and M. Kaess, “InCOpt: Incremental constrained optimization using the Bayes tree,” in *IEEE/RSJ IROS*, 2022.
- [3] M. Kaess, H. Johannsson, R. Roberts, V. Ila, J. Leonard, and F. Dellaert, “iSAM2: Incremental smoothing and mapping with fluid relinearization and incremental variable reordering,” in *IEEE/RSJ ICRA*, 2011.
- [4] I. A. Şucan and S. Chitta, “Motion planning with constraints using configuration space approximations,” in *IEEE/RSJ IROS*, 2012.
- [5] R. M. Eustice, H. Singh, and J. J. Leonard, “Exactly sparse delayed-state filters for view-based SLAM,” *IEEE T-RO*, 2006.
- [6] Z. C. Guo, J. R. Forbes, and T. D. Barfoot, “Marginalizing and conditioning Gaussians onto linear approximations of smooth manifolds with applications in robotics,” in *IEEE/RSJ ICRA*, 2025, pp. 2606–2612.
- [7] M. Kaess and F. Dellaert, “Covariance recovery from a square root information matrix for data association,” *Robotics and Autonomous Systems*, 2009.
- [8] F. Wang and A. E. Gelfand, “Directional data analysis under the general projected normal distribution,” *Statistical methodology*, 2013.
- [9] D. Hernandez-Stumpfhauser, F. J. Breidt, and M. J. van der Woerd, “The general projected normal distribution of arbitrary dimension: Modeling and Bayesian inference,” *Bayesian Analysis*, 2017.
- [10] G. Bourmaud, R. M egret, M. Arnaudon, and A. Giremus, “Continuous-discrete extended Kalman filter on matrix Lie groups using concentrated Gaussian distributions,” *Journal of Mathematical Imaging and Vision*, 2015.
- [11] S. Bonnab e, P. Martin, and E. Sala un, “Invariant extended Kalman filter: theory and application to a velocity-aided attitude estimation problem,” in *IEEE CDC*, 2009.
- [12] P. van Goor, T. Hamel, and R. Mahony, “Equivariant filter (EqF),” *IEEE TACON*, 2022.
- [13] C. Villani *et al.*, *Optimal transport: old and new*. Springer, 2008.
- [14] G. Peyr e, M. Cuturi *et al.*, “Computational optimal transport: With applications to data science,” *Foundations and Trends  in Machine Learning*, 2019.
- [15] P.-A. Absil, R. Mahony, and R. Sepulchre, *Optimization Algorithms on Matrix Manifolds*. Princeton University Press, 2008.
- [16] V. M. Panaretos and Y. Zemel, “Statistical aspects of Wasserstein distances,” *Annual review of statistics and its application*, 2019.
- [17] H. Federer, “Curvature measures,” *Transactions of the American Mathematical Society*, 1959.
- [18] J. M. Lee, *Riemannian manifolds: an introduction to curvature*. Springer Science & Business Media, 2006.
- [19] J.-D. Boissonnat, S. Kachanovich, and M. Wintraecken, “Triangulating submanifolds: an elementary and quantified version of Whitney’s method,” *Discrete & Computational Geometry*, 2021.
- [20] P. Niyogi, S. Smale, and S. Weinberger, “Finding the homology of submanifolds with high confidence from random samples,” *Discrete & Computational Geometry*, 2008.
- [21] R. Vershynin, “High-dimensional probability,” 2009.
- [22] H. Thorisson, “Coupling, stationarity, and regeneration,” *Probability and its Applications*, 2000.
- [23] B. M. Bell and F. W. Cathey, “The iterated Kalman filter update as a Gauss-Newton method,” *IEEE TACON*, 1993.
- [24] J.  esi c, I. Markovi c, and I. Petrovi c, “Mixture reduction on matrix Lie groups,” *IEEE SPL*, 2017.
- [25] J. C. Nascimento, J. G. Silva, J. S. Marques, and J. M. Lemos, “Manifold learning for object tracking with multiple nonlinear models,” *IEEE TIP*, 2014.
- [26] N. J. Gordon, D. J. Salmond, and A. F. Smith, “Novel approach to nonlinear/non-Gaussian Bayesian state estimation,” in *IEE Proceedings F (Radar and Signal Processing)*, 1993.
- [27] M. C. Koval, M. Klingensmith, S. S. Srinivasa, N. S. Pollard, and M. Kaess, “The manifold particle filter for state estimation on high-dimensional implicit manifolds,” in *IEEE/RSJ ICRA*, 2017.